DETC2018-85925

ENERGY HARVESTING FOR NUCLEAR WASTE SENSING AND MONITORING

Yongjia Wu*
Virginia Tech
Blacksburg, VA, USA
Email: yjwu2015@vt.edu

Jackson Klein
Virginia Tech
Blacksburg, VA, USA
Email: jklein3@vt.edu

Hanchen Zhou
Virginia Tech
Blacksburg, VA, USA
Email: hansonz@vt.edu

Lei Zuo
Virginia Tech
Blacksburg, VA, USA
Email: leizuo@vt.edu

ABSTRACT

Monitoring the parameters inside enclosed metal vessels or thick concrete walls as found in dry storage canisters and nuclear reactor vessels is crucial to ensuring safe reactor operation and fuel security. In this paper, two energy harvesters, namely the gamma radiation energy harvester and the thermal energy harvester, were built to power the wireless through-wall and communications for in-situ monitoring of interior conditions in nuclear canisters. The gamma radiation energy harvester was found to have an energy output of 17.8 mW during the first-year canister storage. However, this energy harvester was burdensome, and the performance deteriorates rapidly with time. The thermal energy harvester was thought to be a more practical solution. The power output of the energy harvester was about 93.9 mW in simulation and 46.3 mW in the experiment after 50-years storage in the canister. The power output of this energy harvester can be further scaled by adding TEGs at the cost of larger size.
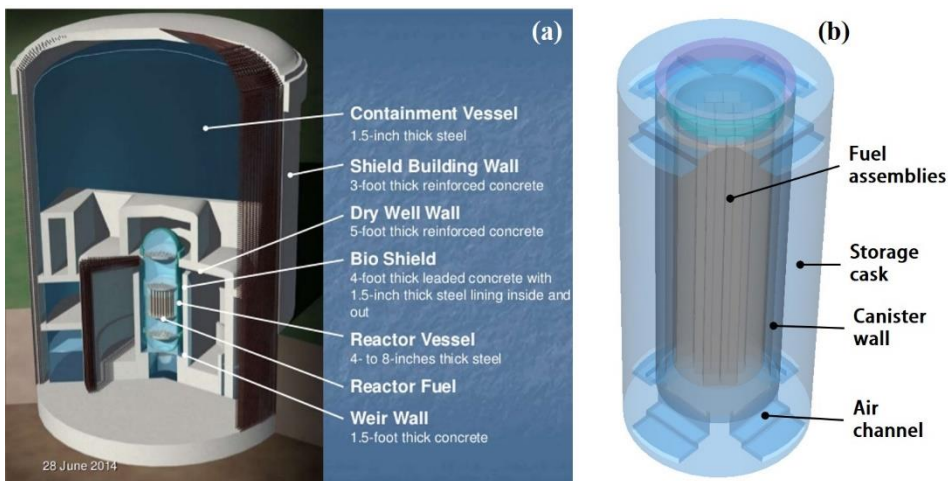
1   Introduction

Figure 1. (a) The enclosed metal wall and thick concrete protection in nuclear reactors [42] and (b) spent fuel dry cask poses challenges in data communications.

Wireless sensors were used in a wide range of civilian and defense applications to provide real-time information about critical parameters, such as temperature, position, pressure, speed, and many others [1-4]. To supply energy to densely populated sensor nodes is a great challenge for the traditional cable system due to the high cost and replacing batteries. Harvesting energy from the sensor's environment is a promising method, and sometimes the only way to operate the sensor [5-7]. The energy sources distributed in the environment include solar light, mechanical vibration or motion, fluid flow, electromagnetic wave, pressure variation, thermal, radiation energies, etc. [8-10]. In most case, the energy densities of these sources are very small. Designing a compact and high-efficiency energy harvester to collect adequate energy to power sensor nodes is no easy task.

In the nuclear industry, many vital components, such as nuclear reactor pressure vessels (RPV) and spent fuel storage canisters (Figure 1), are entirely enclosed by metal and surrounded by thick concrete walls. The reason is to manage the potentially harmful radiation, preventing release to the environment. Taking dry cask storage as an example, typically one-third of the nuclear fuel elements in the reactors are replaced every 18 months, and the U.S. Nuclear Regulatory Commission estimates that 70,000 metric tons of uranium (MTU) is contained in spent fuel. In the U.S. alone, there are 2,100 loaded dry casks, and the number increases by 200 each year. Because radioisotopes resulted from the fission of uranium dioxide (UO_2) in nuclear waste, enough decay heat continues to be produced in spent fuel rods to require them to spend a minimum of one year, and more typically 5 to 10 years, in a spent fuel pool of water, before being further processed

Copyright © 2018 ASME
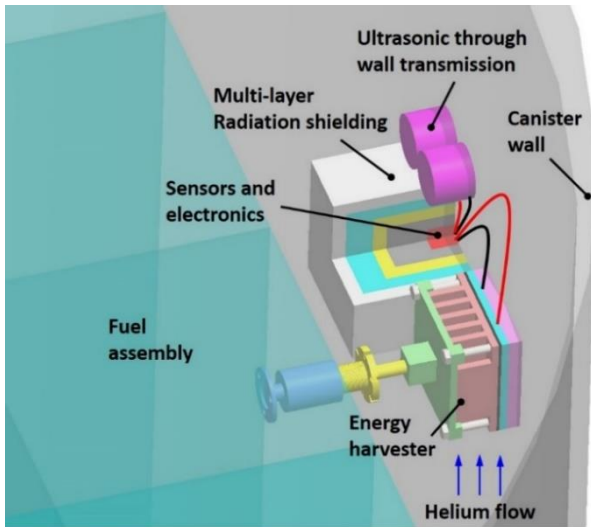
Figure 2. Energy harvesting for sensing and communicating system powering

[11]. The spent nuclear fuel assemblies then will be stored inside (and transported with) containers called canisters surrounded by concrete and steel walls. The canisters are usually lined with leak-tight one-inch thick stainless steel cylinders, providing the front line of protection with a service life of 50 years or longer. Due to long time storage, monitoring temperature, pressure, radiation, humidity, structural health, etc. within these enclosed vessels is crucial to ensure the safety of fuel containment. Because of the potentially volatile nature of the spent fuel, wiring through holes in the vessel walls is undesirable and largely unfeasible in most nuclear environments. This offers a unique problem to harvest energy from the nuclear environment to power the wireless sensors for the canister monitoring.

Energy harvesting and wireless communication (Figure 2) provide a promising opportunity to revolutionize nuclear sensors and instrumentations and to benefit reactor design and fuel cycle facilities by reducing the cost of power, wiring, and signal transmission or eliminating battery replacement. More importantly, when a severe accident or massive loss of grid power happens, the energy harvester can still provide self-sustainable power to monitor the critical parameters of the nuclear power plant or fuel cycle facilities. Clayton et al. [12] gave a comprehensive review of the existing energy sources within the nuclear environment and various energy conversion technologies available for wireless sensor powering. They compared the energy densities of different technologies and pointed out the technology gaps that need to be filled with a workable energy solution being found. Chen et al. [13] presented an on-pipe thermoelectric energy harvester prototype, which can be easily installed on the pipe system to sense the temperature and pressure in the nuclear power plant. The prototype had a maximum open circuit voltage output of 8.06±0.007 V and a maximum power output of 2.25±0.13 W at a source temperature of 246 °C using two thermoelectric modules. Tewolde et al. [14] built a thermoelectrically powered sensing and actuating devices for normal and off-normal conditions in Small Modular Reactors

(SMRs). Zhang et al. [15] developed efficient and reliable TEGs based on high-efficiency nanostructured bulk materials to power WSNs for nuclear application. Carstens et al. [16] described an interesting work using thermoelectric generators to power wireless sensors to monitor spent nuclear fuel stored in a horizontal dry storage container (DSC). The TEG energy harvester was installed in the air channel outside the canister, with the hot end attached to the canister wall and cold side connected to a heat sink. However, the heat flux on the canister wall was assumed to be uniform to calculate the temperature profile within the thermoelectric energy harvester, which might weaken the accuracy of the result. There is still no work done to harvest energy for sensor powering in the thick metal-enclosed canister.

Table 1 below demonstrates the most popular wireless communication technologies, among which ultrasound-based communication provides excellent penetration capacity and reasonable data communication rate. Actually, 10 mW continuous energy harvesting is enough to power a 1.0 W sensing and data transmission system for 3 seconds every 5 minutes.

Table 1. The comparison between different through wall wireless communication technologies

Communication technologies	Ultrasound	EMAT	Inductive
Mechanism	Ultrasound	Ultrasound	Magnetic
Media	Any	Any	Large skin depth
Power (Est.)	~1 watt	~2 watt	~1 watt
Bitrate (Max)	5M bps	1M bps	1000 bps

2 Gamma radiation energy harvesting

2.1 Gamma heat deposited in the tungsten plate

It is well known that all materials will be heated up to a certain degree when placed in ionizing radiation, such as gamma radiation, depending on their material properties. Generally, those with higher densities and thus higher atomic cross sections for scattering will have better absorption ability for gamma rays (outlined by Hubbel and Seltzer in NIST [17]). Tungsten has been selected as the material for gamma heating because of its high material density, 19.25 g/cm^3, and high thermal conductivity, ~170 W/(mK) at 175 °C, making it an ideal candidate to not only absorb maximum gamma radiation, but also transfer the deposited heat to TEGs placed on its surface. In this paper, ORIGAMI embedded in SCALE [18] was first used to calculate the decay heat, gamma and neutron spectrums, and material list after certain-years storage. This information was then used to build a simulation in MCNP6 [19, 20], a Monte Carlo based particle transport simulation which took into account the tungsten plate (20×20×2 cm^3), dry cask geometry, and material make-up, providing the material heating in the tungsten for various years. The simulation was run on a quarter model to save the computational resources, with a tungsten plate placed on the top and another on the side of the fuel assembly, as depicted in Figure 3. A method called geometry splitting was

adopted to accelerate convergence. The simulation was stopped until all statistical checks were well passed by the MCNP6 software and error was less than 5%.

The heating simulation was done for a total of 11 cases, every 5 years from year 5 (start of dry storage) to year 55 (50 years of dry storage) to see the heating effect trend throughout the life of the energy harvester. Shown below in Figure 4 were the results for energy generation due to gamma radiation in the tungsten slabs both at the top of the fuel assembly basket and to the side. Approximately 2.0 W was generated in the tungsten slab above the fuel assemblies, and 1.25 W was generated in the slab beside the assemblies in the first year of dry cask storage. This heat generation dropped quickly in the next 5 years, and eventually, at 50 years in dry storage, there were 200 and 300 mW generated in the side and top slabs, respectively. The deposited heat from neutron heating was calculated to be only about 1.0 mW for the year 5 case [18]. Thus the neutron heating effect was neglected in the following thermal analysis.
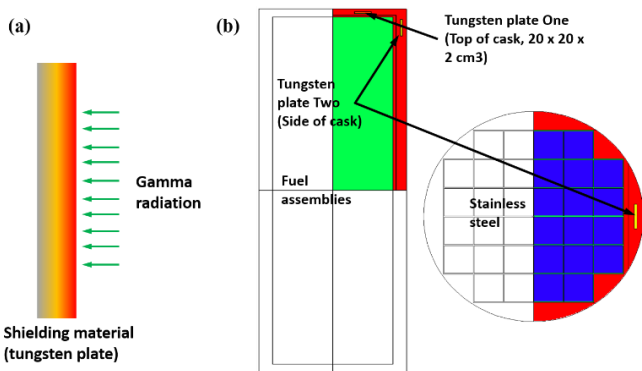

Figure 3. Gamma heating calculation: (a) gamma radiation deposited in tungsten; (b) a quarter model for gamma heating calculation using MNCP6.
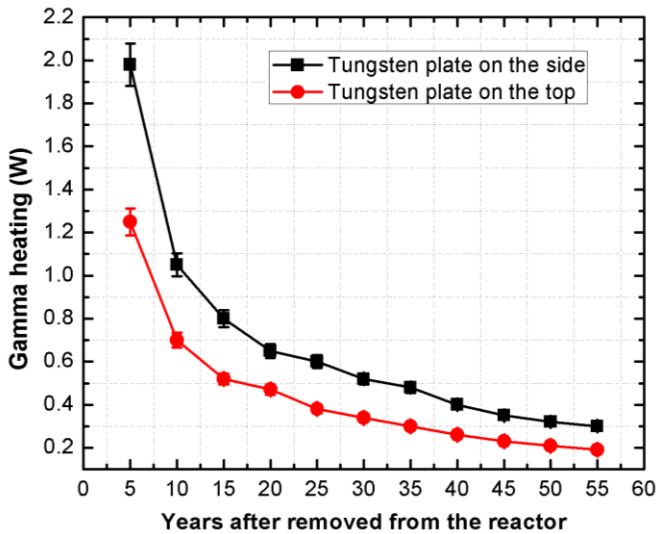

Figure 4. Energy deposited in the tungsten plates at the top and side of the MPC canister for 50 years of dry cask storage.

2.2 Gamma radiation energy harvester

In this section, a concept design that took advantage of only the gamma radiation presented within the canister by heating a tungsten plate was demonstrated. As mentioned in the section above, the maximum gamma deposited heat in a bar of tungsten of $20 \times 20 \times 2$ cm^3 was only about 2.0 W on the top tungsten for the first year of storage in the dry cask. To effectively utilize this small amount of energy, the temperature difference created by the gamma heating should be as large as possible. First, the tungsten should be isolated very well to prevent heat leakage from the hot side of TEGs. Second, the thermal resistance of the TEGs should be large enough to create a high-temperature difference within the module. However, since the tungsten plate had large cross-sectional area and the spreading thermal resistance within the tungsten plate was considerable, it was not easy to effectively isolate the hot side of the energy harvester from the helium environment. What's worse, most of the commercial thermoelectric modules were for high heat flux applications. Their energy conversion efficiencies were pretty small when applied in this situation. Noticing these, we built a gamma heating energy harvester, as depicted in Figure 5, which could effectively use the gamma heating in the tungsten plate.
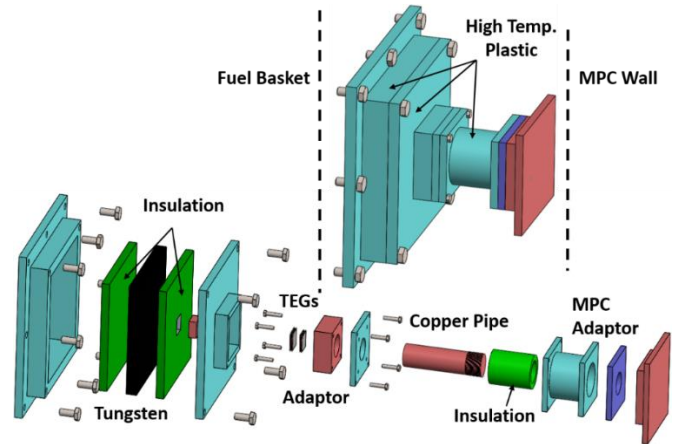

Figure 5. Gamma heating energy harvester design

In this design, the tungsten plate was adapted to the wall of the basket and isolated from the helium gas by high-temperature plastic with very low thermal conductivity. As any material added before the tungsten would cause significant scattering of the gamma particles and result in a reduction in material heating, porous thermal isolation material with extremely low thermal conductivity, such as fiberglass, is good choice to isolate the tungsten plate. To create a high-temperature difference and use the deposited heat effectively, the TEG modules should be stacked thermally in series. The optimum number of the TEGs varies with the thermal isolation condition and the working temperature range of the thermoelectric material. In this design, two HZ-2 TEG (with 196 thermo-elements, Hi-Z Technology, Inc.[21]) modules made of Bi_2Te_3 were used to show the concept. To sink the heat and ensure a temperature drop within the TEGs, the cold end of the second TEG was connected to the cooler

3

canister wall via a backward threaded copper rod. By rotating the threaded rod, the canister wall adaptor would tighten against the canister wall. In this way, the TEGs were thermally connected to the canister wall without the need to mount to the canister. The overall size of the TEG energy harvester was about $30 \times 30 \times 18$ cm^3.

A COMSOL simulation was performed on this harvester to estimate the expected voltage output for the first year of dry storage (year 5 case). The steady-state thermoelectric governing equations for 3-D model embedded in the COMSOL is given by

$$\rho c_p \vec{u} \cdot \nabla T = \nabla \cdot \left(k \nabla T - P \cdot \vec{J} \right) + Q \qquad (1)$$

where ρ is the density, c_p is the thermal capacity, $\vec{u}$ is velocity vector, k is the thermal conductivity, P is the Peltier coefficient, $\vec{J}$ is the current flux vector, and Q is the source term caused by the Joule heat. This model takes account of Peltier effect, Thompson effect, and Joule heat.

The material properties used for thermodynamic analysis were demonstrated in Table 2, among which the properties of thermoelectric materials were cited from the datasheet. The tungsten plate, surrounded by the thermal isolation material, provided an energy source term of 2.0 W, obtained from the MNCP6 simulation. The adaptor surface connected to the cooler canister wall was set to be 410 K, a result of the CFD simulation. In the simulation (Figure 6), assuming the rest of the system was insulated well, a temperature difference of about 18 K was created in the TEG modules, with a corresponding open circuit voltage output of 0.378 V generated in each module. Using the reported value of 4 Ω for the internal electrical resistance in the datasheet [21], the power output with a matched load resistor was thus 17.8 mW, a bit higher than the necessary 10 mW as announced in the section above.

Table 2. Material properties

Material	Electrical resistivity (Ω·m)	Thermal conductivity (W/(m·K))	Seebeck coefficient (V/K)
Bi$_2$Te$_3$ n-type	$1.49 \times 10^{-10}T^2 - 8.66 \times 10^{-8}T + 2.30 \times 10^{-5}$	$-9.52 \times 10^{-6}T^2 + 7.33 \times 10^{-3}T - 0.153$	$-1.12 \times 10^{-9}T^2 + 1.04 \times 10^{-6}T - 5.15 \times 10^{-5}$
Bi$_2$Te$_3$ p-type	$-6.0 \times 10^{-12}T^2 + 6.29 \times 10^{-8}T - 8.79 \times 10^{-6}$	$-1.76 \times 10^{-6}T^2 + 1.39 \times 10^{-2}T - 1.517$	$-3.01 \times 10^{-9}T^2 + 2.387 \times 10^{-6}T - 2.53 \times 10^{-4}$
Copper	6.0×10^{-8}	400	0
Plastic	N/A	0.2	N/A
Tungsten plate	N/A	175	N/A
Thermal isolation	N/A	0.04	N/A
Ceramic covering	N/A	35	N/A

However, because of the huge tungsten plate size and a large volume of thermal isolation material, the final energy harvester was heavy and cumbersome. The tungsten alone had a weight of 26 kg and a size of $20 \times 20 \times 2$ cm^3, making it difficult to be installed and isolated. Also, the thermal isolation material would scatter some gamma rays before it deposited in the tungsten, the gamma heating effect was overestimated in the simulation. Meanwhile, the result presented here was for year 5 case when the gamma heating was highest among all the cases. With times going on, the voltage output and power output of the energy harvester reduced quickly as result of a significant decrease in gamma deposited heat, as shown in Figure 7. For year 55 case, the energy harvester can provide less than 1.0 mW energy, which was far less than 10 mW, a goal we targeted. Considering that at least 10 mW was necessary for the electronics involved in through wall transmission for over 50 years, it was evident that harvesting gamma radiation did not offer a complete solution. However, in the circumstances with higher gamma and neutron radiation fluxes, such as the main containment vessel in the nuclear power plant, gamma heating combined with thermoelectric energy harvester might generate enough energy for sensor powering.
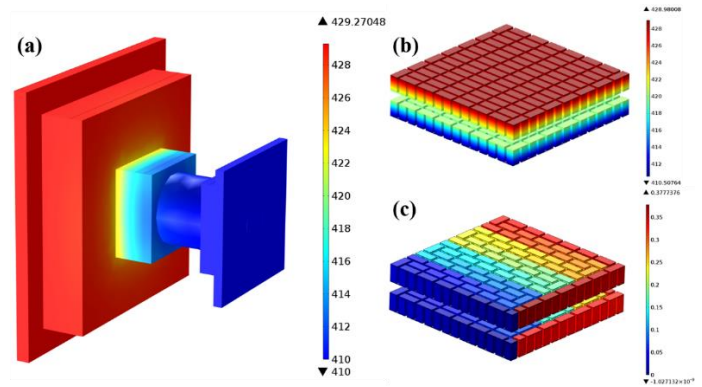

Figure 6. The performance of the gamma heating energy harvester: (a) temperature profile of the energy harvester; (b) temperature profile of the TEGs; (c) electrical potential profile of the TEGs
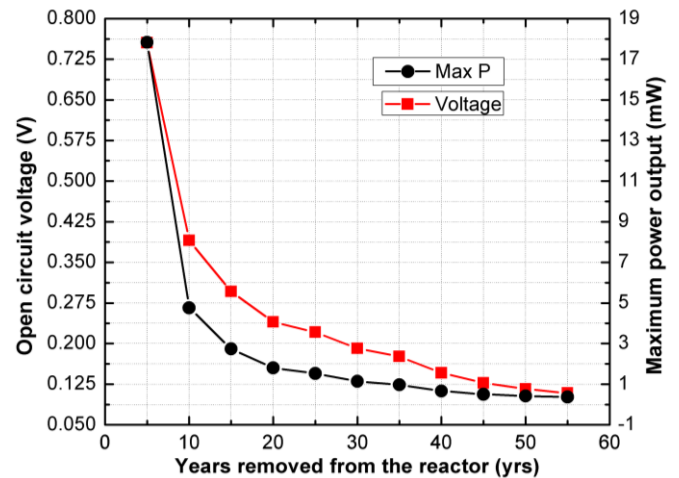

Figure 7. The voltage and power output of the gamma heating energy harvester during 50-years operation

4

Copyright © 2018 ASME

3 Thermal energy harvester

3.1 The thermal energy harvester design

Considering the power output of the gamma radiation energy harvester can hardly meet the power demand (~10 mW) for the wireless communication system, in this section, a more applicable energy harvester to harvest the existing temperature gradient existing near the canister wall was designed. After 50 years of storage in the dry cask, the temperature difference near the canister wall was still as high as 15 K. As the efficiency and power output of the thermoelectric module increase rapidly with temperature difference, it is safe to conclude that, the energy harvester can generate more than enough energy for sensor powering if it can harvest 10 mW averaged power for the year 55 case. In this paper, we designed a simple, compact, and reliable energy harvester which can meet the energy demand for 55-years sensing of the canister, as depicted in Figure 8.

There was a persistent convective flow close to both the basket and canister walls [18]. Here a copper heat sink was designed to improve the convective heat transfer at the hot side of the Bi_2Te_3 TEGs. To be noted that, in this design, there was a tradeoff between the power output, directly correlated to the number of TEG modules, and the overall size of the energy harvester. Thus four TEG1-1263-4.3 modules (256 thermo-elements, TECTEG MFR. [22]) of size $3 \times 3 \times 0.4$ cm^3 were attached to the back of the heat sink. A copper adaptor was mounted to the back of the TEGs to thermally attach them to the cooler canister wall. To make the best use of the space while constraining the device to be relatively small, the following dimensions were used: the fin array base had a length and width of 8 cm to accommodate the four TEGs, the height of each of the fins was 2.5 cm in order to penetrate the flow, and their thickness was constrained to be 5 mm according to the fin optimization result in the following section. The cold side adaptor was curved to fit the contour of the MPC wall and was thin enough such that the entire package had a height of 6 cm. Finally, it was thought that mounting to the MPC wall was undesirable, considering the potential for containment rupture. Thus a mounting rod was positioned, free to rotate, off the end of the finned array, which can be screwed into and out of a base attached to the basket wall. In this way, the harvester can be "clamped" to the MPC canister wall, without the need for mounting to the canister itself, making the design modular, and easy to install. Thin sheets of pliable graphite should be placed between the adaptor and the canister wall to aid in thermal conduction. The overall size of the TEG energy harvester was about $8 \times 8 \times 6$ cm^3, making it compact and easy to install in the canister.
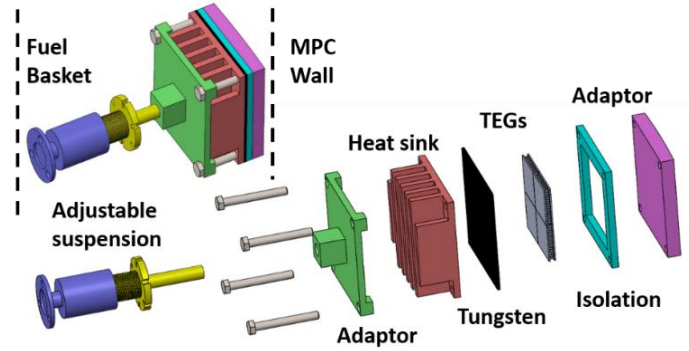

Figure 8. Thermal energy harvester design

3.2 Thermal analysis on the thermal energy harvester

3.2.1 Fin number optimization

To achieve the best performance, the finned array (Figure 9) of the heat sink was optimized based on the flow condition along the canister wall. The dimensions of the baseplate and fin height were taken to be constant, and the fin spacing was varied to optimize the number of fins on the array. The convective heat transfer over the fins was a forced convective flow, and in light of this, optimization was performed accordingly as outlined below.
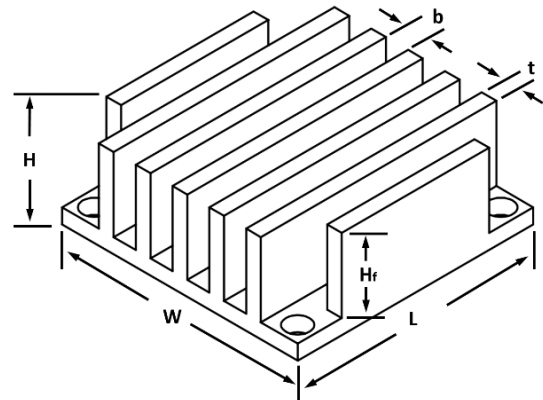

Figure 9. The geometry configuration of a heat sink

Bejan and Sciubba [23] presented a neat method to optimize the fin arrays in a forced convective flow to achieve the best heat transfer performance. In the paper, they gave two approximations to predict the force convective heat transfer rate for narrow and wide fin arrays,

$$\frac{Q_{nc}}{\Delta T} = C_P \left(\frac{\rho W H_f}{1+\frac{t}{b}}\right)\left(\frac{b^2}{12\mu}\right)\left(\frac{P}{L}\right) \qquad (2)$$

$$\frac{Q_{wc}}{\Delta T} = 1.208 \left(\frac{kW H_f}{1+\frac{t}{b}}\right)\left(\frac{PrLP}{\rho v^2 b^2}\right)^{\frac{1}{3}} \qquad (3)$$

where the parameters are illustrated in Figure 9. The pressure drop P in Eqs. (2) and (3) is given below in Eq. (4). It was first theorized by Bejan [23], and then well outlined and condensed in an online publication by Simons [24].

5

$$P = \left(K_c + \frac{4\ F_{app}L}{D_H} + K_e\right)\left(\frac{\rho\ U_{inf}}{2}\right) \quad (4)$$

And F_{app} is given by the following formula, again from Simons [24],

$$F_{app} = \frac{\sqrt{\frac{11.8336}{L_{st}} + (f\ Re_D)^2}}{Re_D} \quad (5)$$

where Re_D is the Reynolds number based on the hydraulic diameter ($D_H = 2b$), $L_{st} = \frac{L}{D_H\ Re_D}$, and f is a polynomial function based on dimensions of the finned structure, and can be found approximated by Simons [24].

Bejan claimed that an approximate solution to the optimum fin number was given by the intersection of the above two heat transfer rates. Here the fin number was calculated using the given fin thickness of 5 mm and assuming the fins fill the base surface. As can be seen, the two approximations for heat transfer rate were plotted for varying fin number and flow velocity. Evidentially, according to this analysis, the crossing point and thus the approximate optimal fin number was between 7 and 8 (Figure 10) and did not vary significantly with decreasing flow velocity.
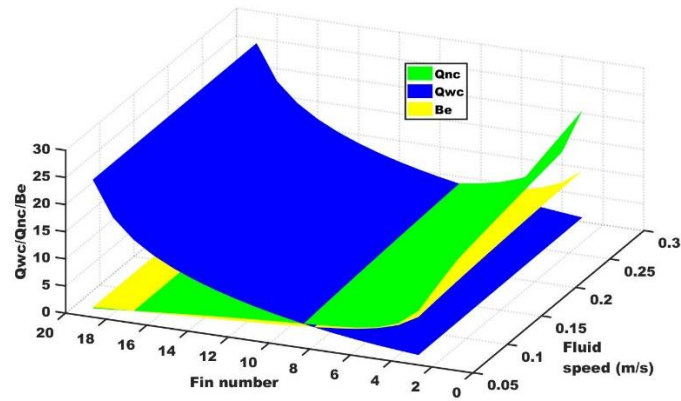

Figure 10. Optimization of fin number for a finned surface placed in the convective helium flow near the MPC wall.

In order to further address the issue, Bejan and Sciubba [23] also presented a numerical analysis to verify this approximation. They concluded that, for optimally spaced finned arrays, the following parameter should be close to 3.0 for flows with a Prandtl number below 0.72 ($Pr = 0.67$ for helium).

$$\delta = \left(\frac{S_f}{L_{hs}}\right)\left(\frac{P\ L_{hs}^2}{\alpha\ \mu}\right)^{\frac{1}{4}} \quad (6)$$

Assuming the Bejan Parameter was equal to 3.0, a simple calculation found that 7 or 8 fins gave the optimal heat transfer rate for this flow, a confirmation of the result in this section above (Figure 10). Thus 7 fins were chosen in this design.

3.2.2 Fluid to simulate the heat transfer performance of the high-pressure helium

In the canister, to enhance the thermal dissipation rate, the canister is backfilled by helium with a pressure of 3.3 atm in MPC-32, whose properties are documented in [25] and listed in Table 3. However, it is hard to duplicate the helium environment in the lab, as the high helium pressure makes the experiment dangerous and helium leakage might happen. The most common fluids in the lab include air, water, and hydraulic mineral oil. Using these fluids to represent helium might achieve the same average convective coefficient as helium by carefully adjusting the flow speed.

Table 3. The thermal properties of different fluids

Fluids	Helium (3.3 atm at 340 K)	Water (1 atm at 340 K)	Air (1 atm at 340 K)	Hydraulic mineral oil (1 atm at 340 K)
μ (N· s/m^2)	2.22e-5	3.69e-4	2.18e-5	1.47e-2
k (W/(m·K))	0.2129	0.67	0.032	0.162
Cp (J/(kg·K))	5195	4092	1010	1670
Pr number	0.67	2.26	0.68	151.6
ρ (Kg/m^3)	0.4121	973.46	1.0	865

The Reynolds number of the helium flow within the fin channel is given by

$$Re_D = \frac{2\rho ub}{\mu} \ll 2300 \quad (u = 0.15\ m/s\ for\ year\ 55) \quad (7)$$

For laminar flow over an isothermal plate, the hydronic boundary layer thickness is

$$\delta_x = \frac{5.0}{\sqrt{u_\infty/vx}} = \frac{5.0x}{\sqrt{Re_x}} \quad (8)$$

In the laminar region, the thickness of the thermal boundary layer is related to the hydronic boundary layer through

$$\frac{\delta_x}{\delta_t} = Pr^{1/3} \quad (9)$$

If there are no interactions between the boundary layers on the different channel surfaces, at the outlet of fin channel, the boundary layer thickness $\delta_L = 27\ mm$, with the corresponding thermal boundary layer thickness $\delta_t = 31\ mm$. Since $\delta_L \gg \frac{b}{2} = 3.25mm$ and $\delta_t \gg \frac{b}{2} = 3.25mm$, the flow in the channel should have been fully developed before it leaves the channel, as illustrated in Figure 11.
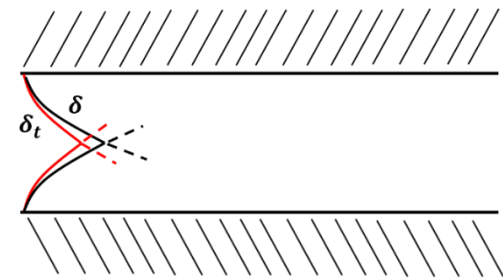

Figure 11. Flow pattern in the fin channel

Muzychka and Yovanovich [26] gave a comprehensive formula to calculate the heat transfer coefficient for laminar forced convective flow in the combined entry region of the non-circular duct. This formula combined the formula to calculate the Nusselt number at the entrance region and formula to predict the Nusselt number for fully developed flow. By introducing some geometry correction for the flow channel, the general model was pronounced to have the ability to evaluate the heat transfer performance for simultaneously developing flow in a duct of

arbitrary cross-sectional shape. A comprehensive examination of this model found that this model was valid for low Reynolds number flow with $0.1 < Pr < \infty$.

$$Nu_{\sqrt{A}} = \left[\left(\frac{C_4 f(Pr)}{\sqrt{z^*}} \right)^m + \left(\left\{ C_2 C_3 \left(\frac{fRe_{\sqrt{A}}}{z^*} \right)^{1/3} \right\}^5 + \right. \right.$$
$$\left. \left. \left\{ C_1 \left(\frac{fRe_{\sqrt{A}}}{8\sqrt{\pi}\epsilon\gamma} \right) \right\}^5 \right)^{m/5} \right]^{1/m} \tag{10}$$

The apparent friction factor $(f_{app}Re_{\sqrt{A}})$ in the entrance region is given by the following formula,

$$f_{app}Re_{\sqrt{A}} = \left[\left(\frac{12}{\sqrt{\epsilon}(1+\epsilon)\left[1 - \frac{192\epsilon}{\pi^5}\tanh\left(\frac{\pi}{2\epsilon}\right)\right]} \right)^2 + \left(\frac{3.44}{\sqrt{z^+}} \right)^2 \right]^{1/2} \tag{11}$$

where
$m = 2.27 + 1.65 Pr^{1/3}$,
$z^+ = \frac{z}{L}/Re_L$,
$L = \sqrt{A}$, and
$z^* = z/LRe_L Pr$.

In this case, the boundary condition can be taken as a uniform wall temperature condition (UWT). The suggested values for the coefficients in Eq. (10) are presented in Table 4.

Table 4. The coefficients for Eq. (10) [26]

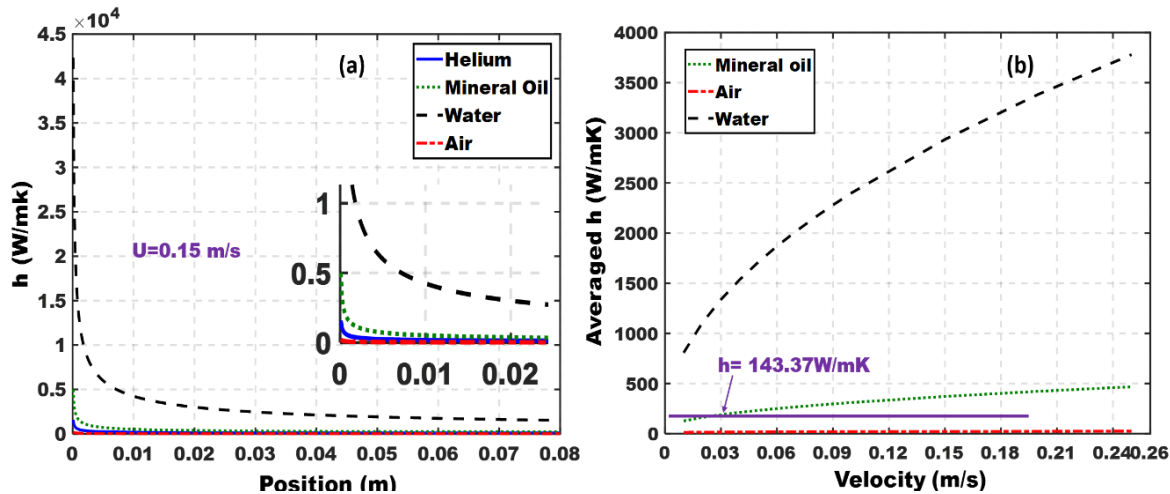|	Boundary condition
UWT	$C_1 = 3.24, C_3 = 0.409$, and $f(Pr) = \frac{0.564}{[1+(1.664 Pr^{1/6})^{9/2}]^{2/9}}$
	Nusselt Number
Local	$C_2 = 1, C_4 = 1, \gamma = 0.1$
Average	$C_2 = 1.5, C_4 = 2, \gamma = 0.1$

Figure 12. Heat transfer performance of different fluids: (a) local heat transfer coefficients when $u = 0.15\ m/s$ and (b) averaged heat transfer coefficients varying with flow speed.

Using this model, we obtained the local and average heat transfer coefficients for air, helium, water, and hydraulic mineral oil, as shown in Figure 12. According to the CFD results, the helium flow went over the heat sink with a fluid speed of 0.15 m/s for year 55 case, with an averaged corresponding heat transfer coefficient of 143.37 W/(m·K). A careful observation of Figure 12 finds that the hydraulic mineral oil can achieve the same averaged heat transfer coefficient of the helium gas by adjusting the inlet flow speed to 1.52 cm/s.

3.2.3 Experiment to test the energy harvester

For year 5 case, the temperature of the flow near the canister wall was as high as 490 K and decreased to 332 K for year 55 case. Four the commercial TEG1-1263-4.3 modules, which can work continuously below 523 K, were connected thermally in parallel and electrically in series to supply power for the 50-years operation of the electronics. As outlined in the above section, the temperature gradient harvestable near the canister wall decreased with time. Thus the energy harvester can meet our energy demand if it can generate enough electricity for year 55 case. In the experiment, we verified the performance of the energy harvester by testing its performance for the year 45, 50, and 55 cases to make sure the energy harvester can supply enough energy during the 55-years operation.

As can be seen in Figure 14, the hydraulic oil circulation loop was used to simulate the helium environment in the canister. The water circulation loop was utilized to control the temperature of the cooling block, which was used to simulate the temperature on the canister wall. The flow rates of the two circulations were controlled by two ball valves and measured by two flow rate meters, respectively. The oil flow was heated up by two 250 W and two 500 W cartridge heaters inserted into a heat exchanger, with their heating rates controlled by a temperature controller. A flow filter was put 10 cm in front of the energy harvester to uniform the flow speed. Three K-type thermocouples were used to measure the hot- and cold- end temperatures of the TEG modules and the temperature of the oil flow. Two data acquisitions (DAQs) from National Instruments Inc. were used to collect the temperature and voltage readings separately. The data was then automatically stored on a PC via LabVIEW every 5 seconds. The experiment was carried out in a room with large space, and the room temperature was constant at 22.5 °C.
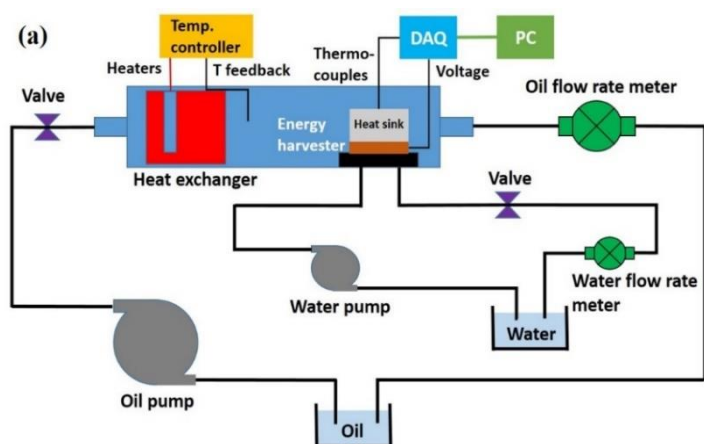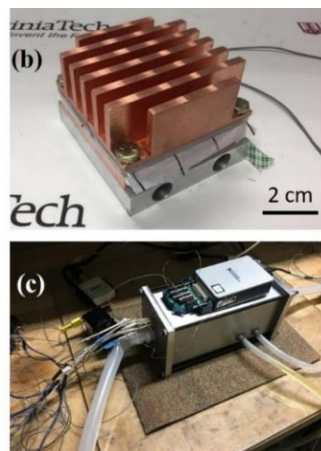
7

Figure 13. The performance test of the energy harvester: (a) The overall experimental setup in the lab, (b) The energy harvester, and (c) the oil channel to simulate the helium environment.

3.2.4 Simulation results

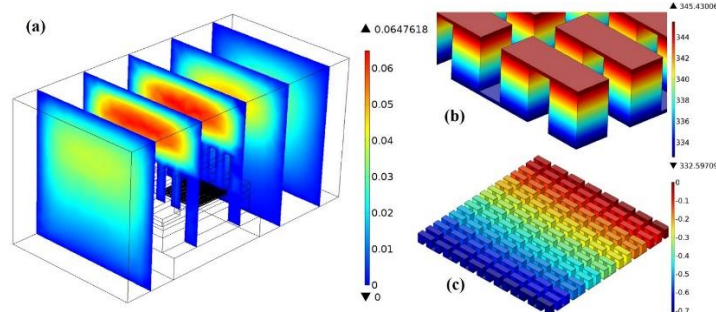**Figure 14.** Simulation of the performance of the thermal energy harvester in hydraulic mineral oil at $u = 0.0152\ m/s$ for year 55 case: (a) fluid speed contours, (b) temperature profile in TEG, and (c) electrical potential profile in TEG.

Known from the analysis above, it was convenient to use hydraulic mineral oil to simulate the convective heat transfer performance of helium gas in the canister. Before the experimental verification, a multi-physics simulation was performed to estimate the voltage and power output of the thermal energy harvester. The thermal properties all the components listed in Table 2 and 3 were used in the simulation. To save some computational resource, only part of the flow region was calculated by appropriately allocating the inlet and outlet. Since the hydraulic mineral oil flow has high viscosity thus low Reynolds number (~12), it does not lose much accuracy to put the inlet 10 cm ahead and the outlet 20 cm back from the energy harvester. The inlet flow was assumed to be uniform with an average speed of 1.52 cm/s as computed in the above section. The inlet flow temperature and the temperature of the cooling block was set according to the CFD results [18]. No thermal and electrical contact resistances were considered in the computations. The multi-physics simulation with heat transfer, thermoelectric, and laminar flow physics models coupled, was done in three grid systems, namely normal, fine, and finer

tetrahedral meshes with their parameters optimized according to the energy harvester geometry.

Demonstrated in Figure 14 was the performance of the thermal energy harvester in hydraulic mineral oil using the finer meshes at $u = 0.0152\ m/s$ for year 55 case. The temperature drop within the thermo-element was about 12.8 K, which was very high considering the total temperature difference is 15 K near the canister wall. The open circuit voltage generated was about 0.712 V for a single TEG. There were four TEGs assembled thermally in parallel. Thus the total voltage output of the energy harvester was 2.848 V. Considering the internal resistance of the TEG module was 5.4 Ω, the maximum power output of the energy harvester was about 93.9 mW, which was more than enough for electronics powering. The results for the different simulation cases were presented in Table 4.

Table 4. The simulation results for different year cases

Cases	Oil temperature (K)	Cooling block temperature (K)	Temperature drop in TEG (K)	Open circuit voltage (V)	Max. power output (mW)
Year 55	347.15	332.15	12.8	0.712	93.9
Year 50	351.15	335.15	13.7	0.757	106.1
Year 45	355.15	338.15	14.5	0.801	118.8

3.2.5 Experimental results

The COMSOL multi-physics simulation gave very promising results to achieve 10 mW energy harvesting taking advantage of the existing temperature difference near the canister wall. An experiment was done in this section to verify the simulation results. The experiment was divided into three periods, with each period lasting for 8 minutes. As shown in Figure 15(a), in the first time period, to simulate the year 55 case, the hydraulic mineral oil was heated up to 347.15 K (74 °C) and the cooling system was preserved to 332.15 K (59 °C), the same as the input value for the simulation. In the second and third periods, the temperatures of the hydraulic mineral oil and the cooling block were adjusted to the values corresponding to different year cases, as demonstrated in Table 4.

As we can see from Figure 15(b), the voltage output changed accordingly with the temperature difference between the hot and cold ends of the TEG module. The voltage outputs of a single TEG module were about 0.50, 0.55, and 0.60 V for the year 55, 50, and 55 cases. In this design, four TEG modules were connected thermally in parallel and electrically in series. The total voltage output of the energy harvester were about 2.0, 2.2,
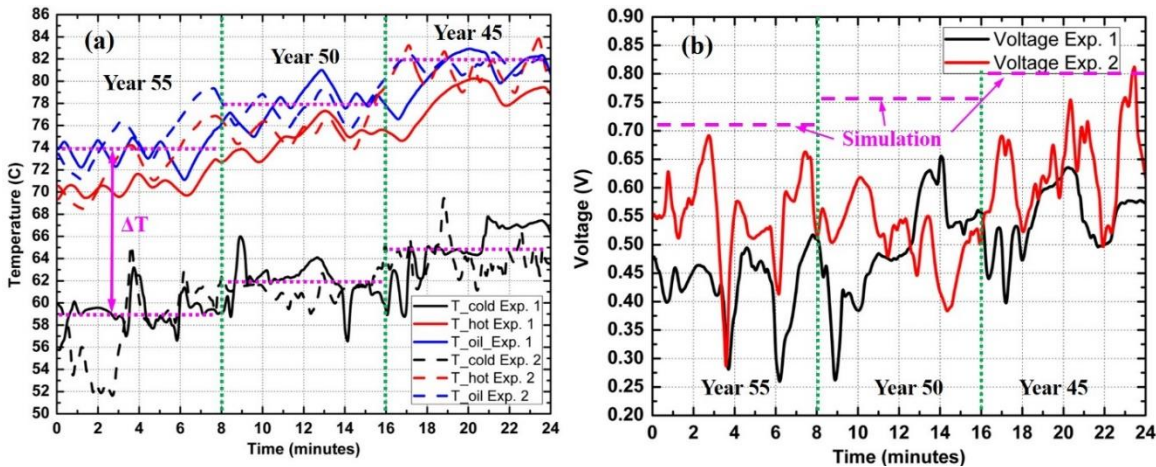
Copyright © 2018 ASME

Figure 15. The experimental results for the thermal energy harvester in hydraulic mineral oil at $u = 1.52\ cm/s$: (a) The hot- and cold- end temperatures of TEG, and flow temperature, and (b) The open circuit voltage output.

and 2.4 V, respectively. The corresponding maximum power outputs of the TEG energy harvester were around 46.3, 56.1, and 66.7 mW, which were more than 10 mW what we need for electronics powering. The performance of the thermal TEG energy harvester was poorer than the simulation result. This can be reasoned as follows. First, the thermal contact resistances were considerable in the energy harvester assembly. Second, the thermal properties of all the material were temperature dependent, especially for the hydraulic mineral oil. Third, though feedback controllers were used to control the temperatures of the oil and the cooling block, the temperature fluctuation during the experiment caused significant derivation in the temperature difference and voltage output.

4   Conclusion

In this paper, we designed two energy harvesters for self-powered wireless through-wall sensing and communicating system in the canister. The first energy harvester was a concept design for the gamma radiation energy harvesting. While the second design harvested thermal energy from the helium flow by taking advantage of the existing temperature difference near the canister wall. After careful thermal analysis and experimental verification, it can be concluded that:

1) In the canister, there are abundant gamma rays. When a tungsten plate ($20 \times 20 \times 2$ cm^3) placed on the side of the canister, a deposited heat of 2.0 W can be achieved for the first-year dry cask storage. However, the gamma deposited heat decreased to about 0.3 W after 50-years storage.

2) A conceptual gamma radiation energy harvester was designed to show the potential using gamma heating effect to power electronics within the canister. Assuming the system was well isolated, the energy harvester, utilizing two TEG modules connected thermally in series and electrically in parallel, gave an ideal voltage output of 0.756 V and a corresponding power output of 17.8 mW. As time went on, the energy harvester can hardly to achieve the goal to harvest 10 mW energy for electronics powering, as a sharp decrease in the deposited gamma heat in the tungsten. Meanwhile, this design was burdensome and huge, providing a practical problem to thermally isolate it and install in in the local site.

3) To further address the energy problem for the wireless communication system, another energy harvester utilizing the existing temperature gradient in the canister was constructed. The heat sink of the energy harvester was optimized according to the flow condition in the canister. Four TEG modules were connected thermally in parallel and electrically in series to harvest enough energy for sensor and communication system powering. The power output of the energy harvester can be easily scaled by adding more TEG modules at the cost of the system size. The thermal energy harvester was simple and compact ($8 \times 8 \times 6$ cm), thus can be easily installed in the local site. To verify the result in the lab, the hydraulic mineral oil was used to simulate the thermal performance of the helium gas in the canister based on a careful thermal analysis.

4) The multi-physics simulation results showed that the energy harvester can supply an open circuit voltage of 2.848 V and energy of 93.9 mW even for the year 55 case (after 50-years fuel storage in the canister), which was more than enough for the electronics powering. However, the experimental results showed that the open circuit voltage and power output of the energy harvester were about 2.0 V and 46.3 mW, respectively, with the same thermal boundary conditions. The difference between the simulation and experimental results can be reasoned by the relatively large thermal resistance at the contact layer and temperature fluctuation during the experiment.

Acknowledgement

Reference

[1] Surie, D., Laguionie, O., and Pederson, T., 2008, "Wireless Sensor Networking of Everyday Objects in a Smart Home Environment," Issnip 2008: Proceedings of the 2008

International Conference on Intelligent Sensors, Sensor Networks, and Information Processing, pp. 189-194.

[2] Hussain, S., Schaffner, S., and Moseychuck, D., 2009, "Applications of Wireless Sensor Networks and RFID in a Smart Home Environment," 2009 7th Annual Communication Networks and Services Research Conference, pp. 153-157.

[3] Akyildiz, I. F., Su, W., Sankarasubramaniam, Y., and Cayirci, E., 2002, "Wireless sensor networks: a survey," Computer networks, 38(4), pp. 393-422.

[4] Chen, J., Klein, J., Wu, Y. J., Xing, S. X., Flammang, R., Heibel, M., and Zuo, L., 2016, "A Thermoelectric Energy Harvesting System for Powering Wireless Sensors in Nuclear Power Plants," Ieee T Nucl Sci, 63(5), pp. 2738-2746.

[5] Priya, S., and Inman, D. J., 2009, Energy harvesting technologies, Springer, New York ; London.

[6] Eu, Z. A., Tan, H. P., and Seah, W. K. G., 2011, "Design and performance analysis of MAC schemes for Wireless Sensor Networks Powered by Ambient Energy Harvesting," Ad Hoc Netw, 9(3), pp. 300-323.

[7] Ulukus, S., Yener, A., Erkip, E., Simeone, O., Zorzi, M., Grover, P., and Huang, K. B., 2015, "Energy Harvesting Wireless Communications: A Review of Recent Advances," Ieee J Sel Area Comm, 33(3), pp. 360-381.

[8] Eiting, C. J., Krishnamoorthy, V., Rodgers, S., George, T., Robertson, J. D., and Brockman, J., 2006, "Demonstration of a radiation resistant, high efficiency SiC betavoltaic," Appl Phys Lett, 88(6).

[9] Knight, C., Davidson, J., and Behrens, S., 2008, "Energy Options for Wireless Sensor Nodes," Sensors-Basel, 8(12), pp. 8037-8066.

[10] Chalasani, S., and Conrad, J. M., 2008, "A survey of energy harvesting sources for embedded systems," Proceedings Ieee Southeastcon 2008, Vols 1 and 2, pp. 442-447.

[11] Ko, J. H., Park, J. H., Jung, I. S., Lee, G. U., Baeg, C. Y., and Kim, T. M., 2014, "Shielding Analysis of Dual Purpose Casks for Spent Nuclear Fuel under Normal Storage Conditions," Nucl Eng Technol, 46(4), pp. 547-556.

[12] Clayton, D. A., Andrews Jr, W. H., and Lenarduzzi, R., 2012, "Power harvesting practices and technology gaps for sensor networks," Oak Ridge National Laboratory (ORNL).

[13] Chen, J., Zuo, L., Wu, Y. J., and Klein, J., 2016, "Modeling, experiments and optimization of an on-pipe thermoelectric generator," Energ Convers Manage, 122, pp. 298-309.

[14] Tewolde, M., Lin, C. C., Tao, H., Chen, H. F., Fu, G. S., Liu, D., Zhang, T., Benjamin, D., Zuo, L., Hwang, D., and Longtin, J., 2014, "Sensors for Small Modular Reactors Powered by Thermoelectric Generators," Proceedings of the Asme Small Modular Reactors Symposium, 2014.

[15] Zhang, Y., Butt, D., and Agarwal, V., 2015, "Nanostructured Bulk Thermoelectric Generator for Efficient Power Harvesting for Self-powered Sensor Networks," Idaho National Laboratory (INL), Idaho Falls, ID (United States).

[16] Carstens, T. A., Corradini, M. L., Blanchard, J. P., Liu, C. H., Li, M., Behdad, N., and Ma, Z. Q., 2013, "Thermoelectric Powered Wireless Sensors for Dry-Cask Storage," Ieee T Nucl Sci, 60(2), pp. 1072-1079.

[17] Hubbell, J., and Seltzer, S., 2004, "Tables of X-ray mass attenuation coefficients and mass energy-absorption coefficients (version 1.4)," National Institute of Standards and Technology, Gaithersburg, MD.

[18] Wu, Y., Klein, J., Zhou, H., and Zuo, L., 2018, "Thermal and fluid analysis of dry cask storage containers over multiple years of service," Annals of Nuclear Energy, 112, pp. 132-142.

[19] Goorley, T., James, M., Booth, T., Brown, F., Bull, J., Cox, L., Durkee, J., Elson, J., Fensin, M., and Forster, R., 2012, "Initial MCNP6 release overview," Nuclear Technology, 180(3), pp. 298-315.

[20] Shultis, J. K., and Faw, R. E., 2011, "An MCNP primer."

[21] Hi-Z Technology, I., 2017, "HZ-2 Thermoelectric Module," http://hi-z.com/product/hz-2-thermoelectric-module/.

[22] TECTEG, 2018, "Specifications TEG Module TEG1-1263-4.3," http://tecteg.com/wp-content/uploads/2014/09/11.pdf.

[23] Bejan, A., and Sciubba, E., 1992, "The Optimal Spacing of Parallel Plates Cooled by Forced-Convection," Int J Heat Mass Tran, 35(12), pp. 3259-3264.

[24] Simons, R., 2003, "Estimating Parallel Plate-fin Heat Sink Pressure Drop," https://www.electronics-cooling.com/2003/05/estimating-parallel-plate-fin-heat-sink-pressure-drop/.

[25] Petersen, H., 1970, "The properties of helium: density, specific heats, viscosity, and thermal conductivity at pressures from 1 to 100 bar and from room temperature to about 1800 K."

[26] Muzychka, Y. S., and Yovanovich, M. M., 2004, "Laminar forced convection heat transfer in the combined entry region of non-circular ducts," J Heat Trans-T Asme, 126(1), pp. 54-61.